Supplementary Information for: One-way electron mirrors from single-layer stacking shifts in rhombohedral graphite

Konrád Kandrai[1, 3, 5], András Balogh[2], Dóra Varga[1, 5], Márton Szendrő[1], András Pálinkás[1], József Cserti[2], János Koltai[2], Krisztián Márity[1, 4, 5], Péter Vancsó[1], Géza I. Márk[1], Alexandre Mayer[6], Zoltán Tajkov[1, 2, 5], Levente Tapasztó[1, 3], and Péter Nemes-Incze[1, 5 *]

[1]Hungarian Research Network, HUN-REN Centre for Energy Research, Institute of Technical Physics and Materials Science, 1121 Budapest, Hungary
[2]ELTE, Eötvös Loránd University, 1117 Budapest, Hungary
[3]Department of Physics, Institute of Physics, Budapest University of Technology and Economics, Műegyetem rkp. 3., H-1111 Budapest, Hungary
[4]Óbuda University, 1034 Budapest, Hungary
[5]MTA - HUN-REN EK Lendület "Momentum" Topology in Nanomaterials Research Group
[6]Department of Physics, Namur Institute for Complex Systems (naXys), University of Namur, Namur, Belgium

[*] *corresponding author, email: nemes.incze.peter@ek.hun-ren.hu*

October 21, 2026

Contents

S1 Electronic Raman scattering on the sample **2**

S2 Further examples of interference fringes **4**

S3 Implementation of doping in the tight-binding model **6**

S4 Electron–hole asymmetry in the interference fringes **6**

S5 WPD calculation details **9**
S5.1 WPD calculation geometry 9
S5.2 WPD calculation videos 9
S5.3 Reflection probability for a graphene contact to the bottom graphene layer . 12

S6 Minimal scattering model: reciprocity and mode selection **13**

S1 Electronic Raman scattering on the sample

The stacking order of the sample area measured in the main text was verified by electronic Raman scattering (ERS); for the method see Ref. [1]. In Fig. S1 we compare the ERS peaks of a defect-free area with ABC stacking, the $(+^5)$ structure, and of a $(+^4-)$ stacking fault area. Using conductive atomic force microscopy (AFM) images and comparing them with the STM dI/dV maps, we located the area shown in the figure panels of the main text. The Raman spectrum of this area, shown in purple in Fig. S1, exhibits the ERS peaks of both the $(+^5)$ and the $(+^4-)$ stacking sequences. Measurements with crossed polarizers transmit the ERS signal, while measurements with parallel polarizers (blue spectrum in Fig. S1) filter it out and leave only the phonon peaks. The ERS spectra were recorded with a Witec 300rsa+ confocal Raman system at 488 nm laser excitation, using a diffraction grating with 600 lines per mm. The spectra were first processed with the Witec data processing software supplied with the system. Final data processing and the figure were produced with the open-source Python tool Ramantools [2].

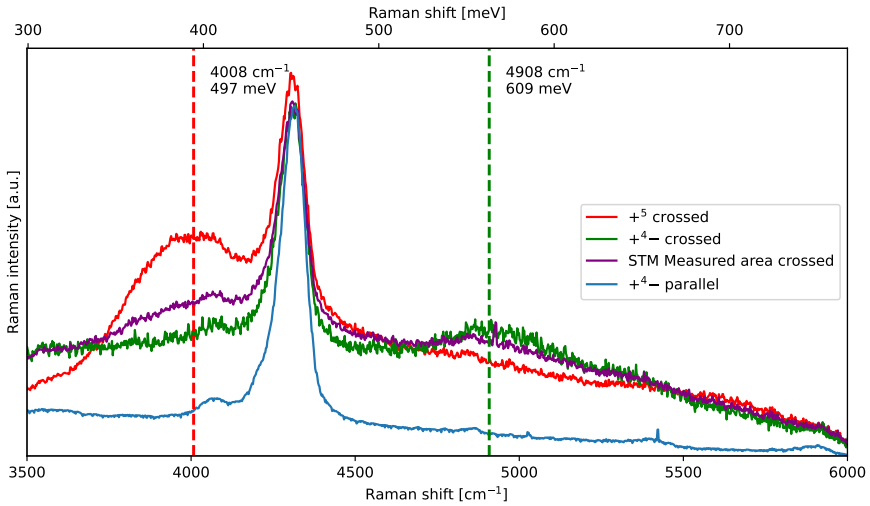


Figure S1: **Electronic Raman scattering (ERS) of the sample.** High-wavenumber Raman spectra of large, pure $\left(+^5\right)$ (red) and $\left(+^4-\right)$ (green) domains show the $-1 \rightarrow +1$ ERS transitions at 4008 cm^{-1} and 4908 cm^{-1}, respectively. The spectrum recorded on the area with multiple domain walls (purple) is a mixture of the spectra of the two pure domains. The FWHM diameter of the laser spot (∼500 nm) is larger than the width of the domains in the area mapped by STM, which explains the mixed ERS signal. With a second, parallel polarizer (analyzer) the complete ERS signal is filtered out (blue), leaving the high-wavenumber phonon peaks (3D, 2D+G, 3D', 4D and 2D+2G around 4050, 4300, 4850, 5400 and 5880 cm^{-1}) clearly resolved.

S2 Further examples of interference fringes

Here we present further examples of dI/dV spectra along lines, measured perpendicular to the domain walls separating the $(+^5)$ and $(+^4-)$ regions. Measurements of the sample bias dependence of the interference fringe wavelength in these measurements also fit the Dirac band dispersion of the $(+^4-)$ structure.

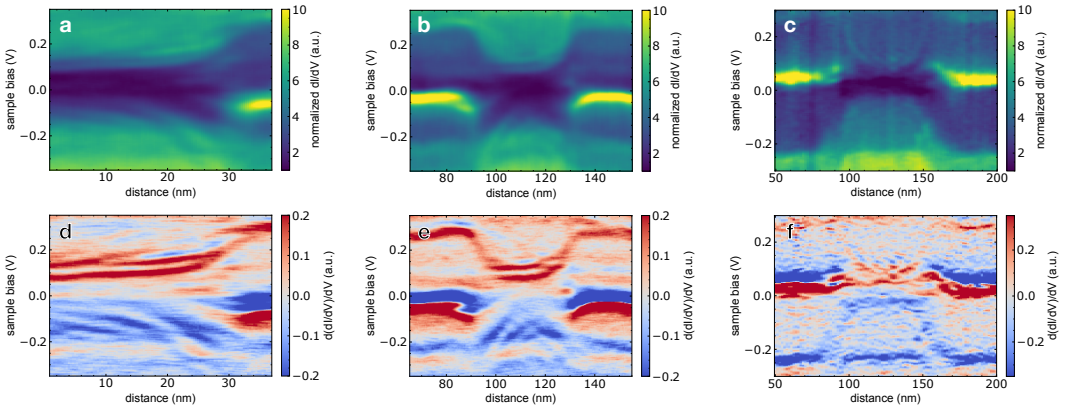


Figure S2: **Further examples of quasiparticle interference in dI/dV spectra along a line. (a-c)** Differential conductance (dI/dV) line spectra measured along domain transitions. **(d-f)** Numerical derivative of the dI/dV line spectra shown above each panel, with respect to the sample bias. Panels a and d have defect free $(+^5)$ area on the rightmost side, while other panels have a similar nanoribbon-like geometry of the $(+^4-)$ area, as the data presented in the main text. Panels c and f feature doping in which the flat-band is unoccupied. The domain wall angle to the zigzag direction is 20° for panels b/e and 14° for panels c/f.

The absence of fringes in the $(+^5)$ region, also at the energies of the flat band, is shown for a thin RG ribbon in Fig. S3, together with the corresponding tight-binding calculation.

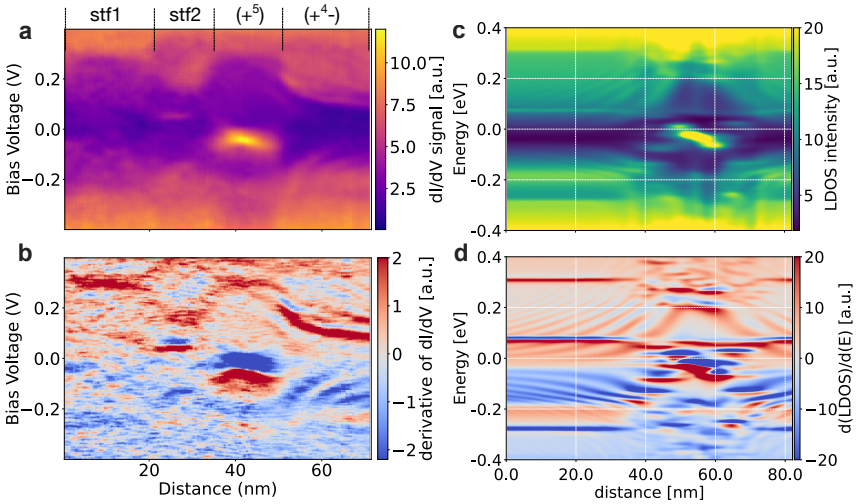


Figure S3: **Spatially resolved spectroscopy of a rhombohedral graphite nanoribbon. (a)** dI/dV line spectra acquired along a line crossing a rhombohedral graphite (RG) nanoribbon. The areas with known stacking are highlighted. There are two unidentified stacking sequences, with a hexagonal character at the top surface (no flat band), denoted by *stf1* and *stf2*. **(b)** Numerical derivative of the dI/dV line spectra with respect to the sample bias, enhancing the visibility of spectral features. There are no clear interference fringes in the *stf1* and *stf2* regions, only in the $(+^4-)$ region. **(c)** Calculated surface LDOS for an RG nanoribbon based on our tight-binding (TB) model, showing the interference fringes in the $(+^4-)$ area. **(d)** Energy derivative of the calculated LDOS in c, facilitating direct comparison with the experimental data in b.

S3 Implementation of doping in the tight-binding model

Apart from the hopping terms explained in the main text we used additional on-site terms to take into account the doping coming from the charge inhomogeneities on the SiO_2 substrate. Using DFT calculations this inhomogeneity can be modeled as placing a charged plane below the system and calculate the electronic structure with the extra positive or negative charge on this plane. Due to the asymmetry of the doping profile, the on-site terms are not uniform, in each layer they depend on that given layer and the substrate's distance. We found that this dependence is exponential and the on-site term in layer N has the following form:

$$\Delta_N = A_0 \exp[-\alpha(7 - N)] + b, \tag{S1}$$

In the equation above N is the number of the layer and the numbering starts with 1, which is the top layer seen by the STM tip and goes to 6, the layer closest to the substrate. The parameters A_0 and α determine the strength and decay length of the doping respectively, the on-site term being largest in the layer closest to the substrate and decaying toward the top layer. The constant energy shift b does not depend on the position of the layer. The value of the three parameters, A_0, α and b was fitted to the positions of the peaks in the dI/dV spectra originating from the flat-band side-bands in the band structure of ABC hexalayer graphene.

S4 Electron–hole asymmetry in the interference fringes

One result of the slight surface doping is the electron–hole asymmetry in the observed interference fringes. In the experimental dI/dV line scans, this asymmetry shows in how well the fringes develop on the two sides of the Fermi level. When the flat band lies below the Fermi level, the hole-side fringes are better developed; when it lies above, the electron-side (positive sample bias) fringes are clearer. This asymmetry results from the substrate-induced doping: our TB calculations for the undoped system show no such asymmetry. We attribute it to a small wave-function weight of the bottom flat band (the one next to the substrate) appearing on the top surface, which is what the STM probes. This weight arises because

the bottom flat band acquires a non-negligible dispersion owing to the doping from the SiO_2 substrate. It appears as a small peak on the opposite side of the Fermi level from the main top-surface flat band. The same feature is present in the $\left(+^4-\right)$ stacking fault region, as marked by the black arrows in Figs. 1 and 2 of the main text. This LDOS peak obscures the interference fringes near the energy at which it appears. The sample doping most likely originates from charged impurities in the SiO_2 substrate[3]. Such doping of the layers closest to the substrate also occurs, and has to be taken into account, for hBN-supported samples[4].

Figure S4 presents TB calculations for zero doping and for p-doping, where the flat band is unoccupied (for a corresponding measurement see Fig. S2c,f). In the latter case, the faint trace of the bottom flat band on the surface, caused by the doping, is visible at small negative energies below the Fermi level. Taking the substrate-induced doping into account explains the "gap" feature next to the flat-band peak, which has also been observed by other groups[5].

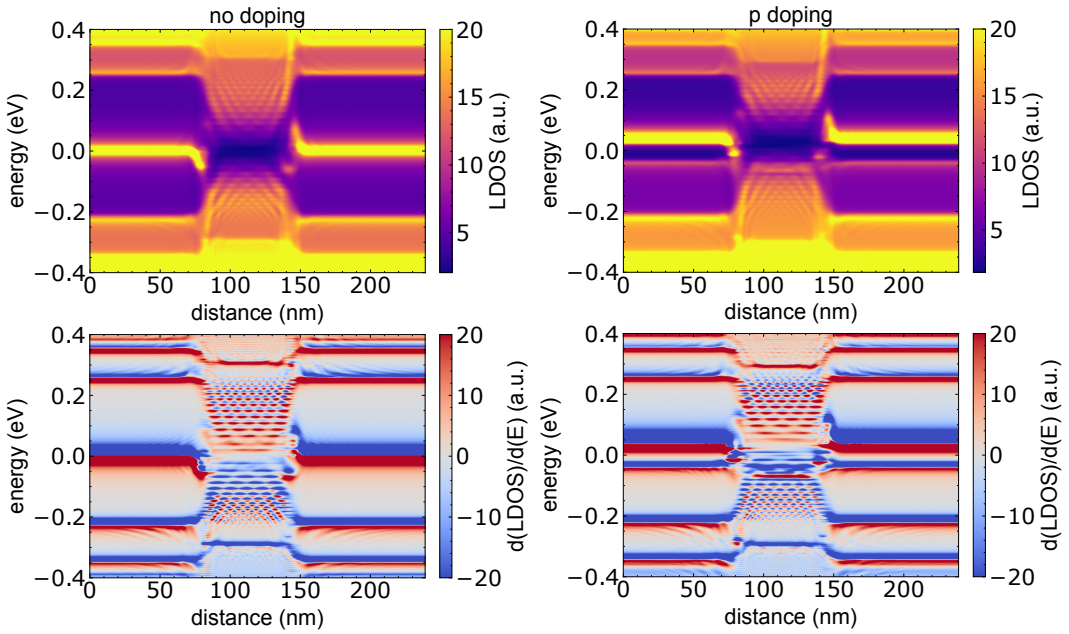


Figure S4: **Calculated energy-dependent LDOS maps along a line, for no doping and for doping of the opposite sign to that in the main text. (Top Left)** LDOS along a line, calculated with the tight-binding (TB) model for an RG nanoribbon, without doping. **(Bottom Left)** Energy derivative of the calculated LDOS above (the energy corresponds to the sample bias in the experiment), facilitating direct comparison with the experimental data. **(Top Right)** LDOS along a line, calculated with the TB model for an RG nanoribbon, with doping of the opposite sign. **(Bottom Right)** Energy derivative of the calculated LDOS above.

S5 WPD calculation details

The WPD method provides the time-dependent wave function $\psi(\vec{r};t)$ by solving the time-dependent Schrödinger equation[6]. Its inputs are the potential $V(\vec{r})$ describing the system and the initial wave function $\psi_0(\vec{r}) = \psi(\vec{r};t=0)$. A time–energy Fourier transform also provides the energy-dependent wave function $\psi(\vec{r};E)$. In our calculation the initial wave packet, starting from the single layer graphene lead (see Fig. S5), is constructed from the Bloch states of graphene around the K point by a Gaussian convolution. The potential $V(\vec{r})$ is our recently developed pseudopotential[7]. The functional form of the pseudopotential is a sum of Gaussians centered on the atomic sites, and its parameters are given in Ref.[7]. The atomic structure is specified in the following subsection.

S5.1 WPD calculation geometry

Figure S5 shows the geometry used in the wave packet dynamics calculations. The wave packet starts in the single layer graphene lead with probability $p_{\text{in}} = 1$ and propagates toward the junction; the probability returning into the lead, p_{out}, gives the reflection. For $\left(+^5\right) \to \left(+^4-\right)$ incidence the reflection is negligible, whereas for $\left(+^4-\right) \to \left(+^5\right)$ incidence it is strong (Fig. 4c of the main text). The model geometry and the initial wave packet are infinite, that is, periodic in the x direction. The width of the calculation box is only $3a_{\text{CC}}$ in the x direction ($3a_{\text{CC}}$ is the armchair periodicity of graphene), with periodic boundary conditions applied in this direction. The layers are displaced progressively by a_{CC} along x, the armchair direction; in the $\left(+^4-\right)$ structure the top layer is displaced in the opposite direction. The structure is relaxed by molecular statics in LAMMPS, see the Methods section of the main text.

S5.2 WPD calculation videos

The time evolution of the wave packet incident on the domain wall from the two sides is shown in Supplementary Video 1 and Supplementary Video 2. Both videos show a side view of the junction, with the same presentation. The six black bars symbolize the six graphene layers; their thickness corresponds to the lateral extent of the σ orbitals. The

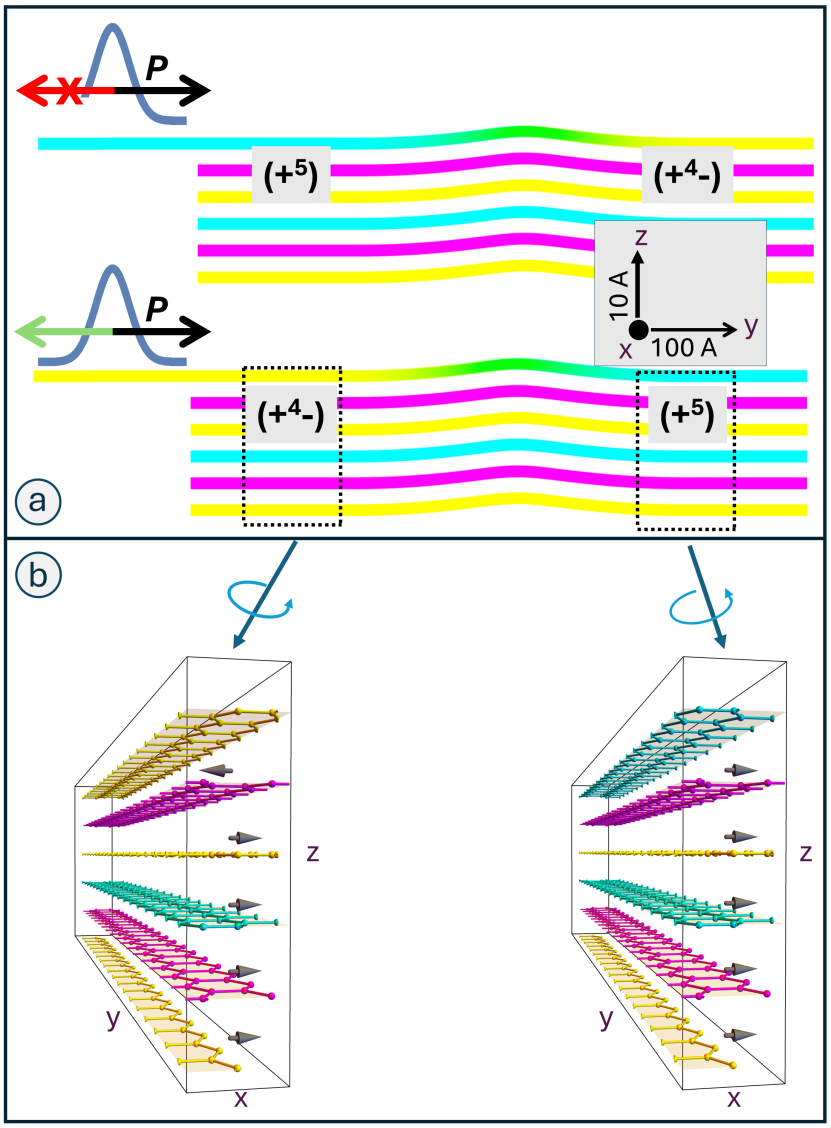


Figure S5: **Model geometry of the wave packet dynamics calculation. (a)** yz cross section of the six-layer structure, the layers color coded by their lateral displacement (yellow, magenta and cyan for A, B and C). The wave packet (blue Gaussian) starts in the single layer graphene lead (black arrow, $p_{\text{in}} = 1$); the reverse arrows mark the reflected probability p_{out}: negligible for $\left(+^5\right) \to \left(+^4-\right)$ incidence (crossed-out red arrow), finite for $\left(+^4-\right) \to \left(+^5\right)$ incidence (green arrow). The y and z scales differ by a factor of 8, to show the z protrusion of the soliton; the width of the wave packet is not to scale. **(b)** Three-dimensional view of the sections marked by dotted rectangles in a; the gray arrows show the displacement of successive layers by a_{CC} along x, reversed for the top layer of the $\left(+^4-\right)$ structure. Colors as in a.

animations show the time development of the probability density $\varrho(\vec{r};t)$ of the wave packet, constructed from the π orbitals of graphene around the K point. Black is zero probability, bright magenta is maximum probability. The color scale is the same for each panel and it is clipped at the high end, to visualize both the large probability density of the narrow initial wave packet and the small probability density of the wave packet after it has spread out. The presentation window has free-space boundary conditions on its left and right sides; a wave packet reaching these boundaries leaves the window, so the window is slowly depleted. In this two-dimensional side view we display the integral $\int \varrho(x,y,z;t)\,\mathrm{d}x$ of the three-dimensional probability density, with a slight smoothing applied in the y direction to wash out the atomic-scale oscillations. The wave packet first moves on the single layer graphene lead with negligible dispersion, because of the linear dispersion of graphene near the K point. Upon reaching the six-layer region, at $t = 5$ fs, a scattering event occurs: part of the wave packet is reflected back into the single layer graphene, another part begins to propagate in the six-layer region.

Supplementary Video 1 shows the effect of the stacking domain wall. The two upper panels show the system with the domain wall, the two lower panels the system without it, that is, a semi-infinite six-layer region with $\left(+^5\right)$ (lower left) and $\left(+^4-\right)$ (lower right) stacking. The two columns differ in the direction of incidence: from $\left(+^5\right)$ toward $\left(+^4-\right)$ in the left column and from $\left(+^4-\right)$ toward $\left(+^5\right)$ in the right column. In the two lower panels the wave packet propagates to the right, bounces between the layers, spreads out and eventually leaves the presentation window on the right side. In the $\left(+^4-\right) \to \left(+^5\right)$ case (upper right panel) part of the wave packet is reflected upon reaching the domain wall, as marked by a white ellipse at $t = 68$ fs, and begins to propagate back toward the single layer region. It reaches the single layer graphene lead at $t = 108$ fs and eventually leaves the presentation window on the left side. There is no discernible reflection from the domain wall in the $\left(+^5\right) \to \left(+^4-\right)$ case (upper left panel).

Supplementary Video 2 shows the effect of the injection layer on the reflection asymmetry. The two left (right) panels show injection into the top (bottom) graphene layer, while the two rows differ in the direction of incidence: from $\left(+^5\right)$ toward $\left(+^4-\right)$ in the upper row and from $\left(+^4-\right)$ toward $\left(+^5\right)$ in the lower row. When the wave packet injected into the top

layer reaches the domain wall from the $(+^4-)$ side (lower left panel), a considerable part of it is reflected, as marked by a white ellipse at $t = 68$ fs, and begins to propagate back toward the single layer region. It reaches the single layer graphene lead at $t = 108$ fs and eventually leaves the presentation window on the left side. There is no discernible reflection from the domain wall in the other three panels, neither for incidence from the $(+^5)$ side, nor for injection through the bottom graphene layer.

S5.3 Reflection probability for a graphene contact to the bottom graphene layer

In Fig. S6 we compare the energy-resolved reflection probabilities calculated for two positions of the graphene lead. The left panel of Fig. S6 shows the reflection probability when the graphene lead is connected to the top graphene layer. In this case we see a clear and strong reflection asymmetry for energies within the RG gap. The right panel of Fig. S6 shows the reflection probability calculated with the graphene lead connected to the bottom graphene layer. In this case there is still some reflection asymmetry at certain energies, but the difference is not as pronounced as with the top-layer lead, showing that the asymmetry relies on the mode selection by the top-layer contact discussed in Section S6.

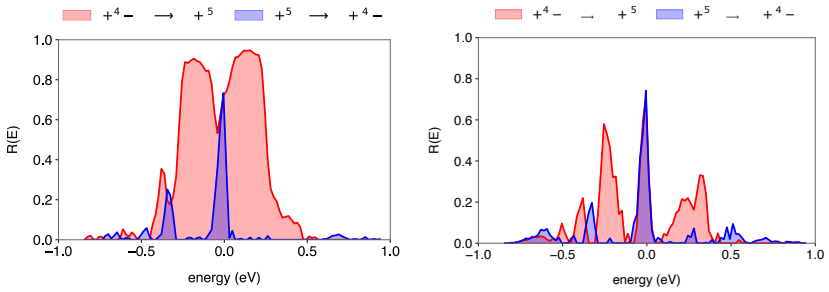


Figure S6: **Comparing reflection probabilities for top- and bottom-layer leads.** Left panel: the same data as in Fig. 4c of the main text, for comparison with the right panel. Here the graphene lead is connected to the top graphene layer, which is probed by the STM tip (layer 1 in Fig. 3 of the main text). Right panel: reflection probability with the graphene lead connected to the bottom graphene layer (layer 6 in Fig. 3 of the main text).

S6 Minimal scattering model: reciprocity and mode selection

Here we show, in a simple one dimensional model, how a scatterer that is linear (its response does not depend on the wave amplitude), energy conserving and time-reversal symmetric reflects asymmetrically when it is probed through a subset of its modes, and how this maps onto the one-band versus two-band case at the $\left(+^5\right)$ - $\left(+^4-\right)$ domain wall. The model and its solution are shown in Fig. S7.

For a one dimensional chain, with a single propagating mode on each side, containing a scatterer, the scattering matrix is 2×2,

$$S = \begin{pmatrix} r & t' \\ t & r' \end{pmatrix}, \tag{S2}$$

with r and r' the reflection amplitudes for waves arriving from the left and from the right, and t and t' the corresponding transmission amplitudes. Unitarity of S, that is flux conservation, requires $|r|^2 + |t|^2 = 1 = |r'|^2 + |t'|^2$ and $|t| = |t'|$, hence

$$|r|^2 = |r'|^2 \tag{S3}$$

for any barrier and without invoking time-reversal symmetry. Directional reflection asymmetry therefore needs at least two propagating modes on one side of the boundary. Two modes on one side and one on the other is equivalent to a three-terminal scatterer: each propagating mode is a terminal, and the 3×3 scattering matrix of the junction is that of three single-mode leads meeting at a point. For a three-terminal scatterer it is no surprise that the reflections seen from two of the terminals differ in the general case. If a third terminal is present, it carries away different fractions of the flux injected from the other two, and only a symmetry that exchanges the two terminals, or a decoupled third terminal, can force the two reflections to be equal.

The minimal lattice realization of this three-terminal structure is a semi-infinite chain (hopping $-t$, one mode, L) joined to a semi-infinite two-leg ladder (leg hopping $-t$, rung

hopping $-t_\perp$, two modes), Fig. S7a. The end site of the chain couples to the two legs A and B of the first rung with hoppings $-\tau_A$ and $-\tau_B$. Because the two legs are identical, the eigenstates of every rung are the symmetric (bonding) and antisymmetric (antibonding) combinations of the wave-function amplitudes $\psi_A(n)$ and $\psi_B(n)$ on the two legs, $\psi_b(n) = [\psi_A(n) + \psi_B(n)]/\sqrt{2}$ and $\psi_{ab}(n) = [\psi_A(n) - \psi_B(n)]/\sqrt{2}$. The ladder therefore carries two independent modes, b and ab, with dispersions $E = \mp t_\perp - 2t\cos k$. In this basis the junction is three single-mode chains meeting at one site. The end site of the chain couples to the first rung through the combination $\tau_A\psi_A(1) + \tau_B\psi_B(1)$, which in the mode basis reads $g_b\psi_b(1) + g_{ab}\psi_{ab}(1)$, with

$$g_b = \frac{\tau_A + \tau_B}{\sqrt{2}}, \qquad g_{ab} = \frac{\tau_A - \tau_B}{\sqrt{2}}. \tag{S4}$$

Written out, the Hamiltonian in this basis is

$$\begin{aligned} H = & -t \sum_{n\le -1} \big(c_L^\dagger(n)\, c_L(n+1) + \text{h.c.}\big) \\ & + \sum_{n\ge 1} \Big[-t\big(c_b^\dagger(n)\, c_b(n+1) + \text{h.c.}\big) - t_\perp\, c_b^\dagger(n)\, c_b(n) \Big] \\ & + \sum_{n\ge 1} \Big[-t\big(c_{ab}^\dagger(n)\, c_{ab}(n+1) + \text{h.c.}\big) + t_\perp\, c_{ab}^\dagger(n)\, c_{ab}(n) \Big] \\ & - g_b\big(c_b^\dagger(1)\, c_L(0) + \text{h.c.}\big) - g_{ab}\big(c_{ab}^\dagger(1)\, c_L(0) + \text{h.c.}\big), \end{aligned} \tag{S5}$$

where $c_\sigma(n)$ annihilates a particle on site n of chain σ. The first three terms are three semi-infinite single-mode leads, L, b and ab, and the last two join them at a single site: the junction is a three-terminal scatterer. Its scattering matrix relates the outgoing to the incoming wave amplitudes in the three leads, $(o_L, o_b, o_{ab})^T = S\,(i_L, i_b, i_{ab})^T$. In block form, with rows and columns ordered (L, b, ab),

$$S = \left(\begin{array}{c|cc} S_{LL} & S_{Lb} & S_{L,ab} \\ \hline S_{bL} & S_{bb} & S_{b,ab} \\ S_{ab,L} & S_{ab,b} & S_{ab,ab} \end{array}\right), \tag{S6}$$

where the 1×1 block S_{LL} is the reflection amplitude on the chain side, the 2×2 block contains

the reflection amplitudes S_{bb} and $S_{ab,ab}$ on the ladder side and the conversion $S_{b,ab} = S_{ab,b}$ between its two modes, and the off-diagonal blocks are the transmission amplitudes across the junction[8]. Both properties follow from the Hamiltonian: its Hermiticity conserves the flux and makes S unitary, and its real hoppings make the model time-reversal symmetric and S symmetric, $S = S^T$ [9–11].

We now show that reciprocity constrains the transmissions between the three terminals, but not the reflections seen by a probe that couples to only two of them. This selective coupling is what happens in the case of the STM measurement: the tip couples to the dispersive part of the $\left(+^5\right)$ region and the Dirac cone of the $\left(+^4-\right)$. Let $R_L = |S_{LL}|^2$ and $R_b = |S_{bb}|^2$ be the reflection probabilities of a wave injected in mode L and in mode b, and $T_{i\to j} = |S_{ji}|^2$ the transmission probabilities. Unitarity gives the sum rules $R_L + T_{L\to b} + T_{L\to ab} = 1$ and $R_b + T_{b\to L} + T_{b\to ab} = 1$, and $S = S^T$ gives $T_{L\to b} = T_{b\to L}$. Subtracting the two sum rules,

$$R_b - R_L = T_{L\to ab} - T_{b\to ab}. \tag{S7}$$

Reciprocity equates the two directions of every transmission, $T_{i\to j} = T_{j\to i}$, and allows the two reflections to differ, by exactly the difference in what leaks into the channel the probe does not see. The identity uses only unitarity and $S = S^T$, so it holds for any junction. If several channels are hidden from the probe, on either side of the boundary, the right-hand side becomes a sum over them. If $g_{ab} = 0$ the ab channel decouples and Eq. (S3) forces $R_L = R_b$, making the junction a two-terminal system. Coupling to a channel invisible to the probe is what enables the reflection asymmetry. For the ladder the reflection amplitudes follow from Eq. (S5) with plane waves $e^{\pm ik_\sigma n}$ in the three leads, where $0 < k_\sigma < \pi$ are the wavenumbers of the three channels at energy E:

$$\begin{aligned} S_{LL} &= \frac{g_b^2 e^{ik_b} + g_{ab}^2 e^{ik_{ab}} - t^2 e^{ik_L}}{D}, \\ S_{bb} &= \frac{g_b^2 e^{-ik_b} + g_{ab}^2 e^{ik_{ab}} - t^2 e^{-ik_L}}{D}, \\ D &= t^2 e^{-ik_L} - g_b^2 e^{ik_b} - g_{ab}^2 e^{ik_{ab}}. \end{aligned} \tag{S8}$$

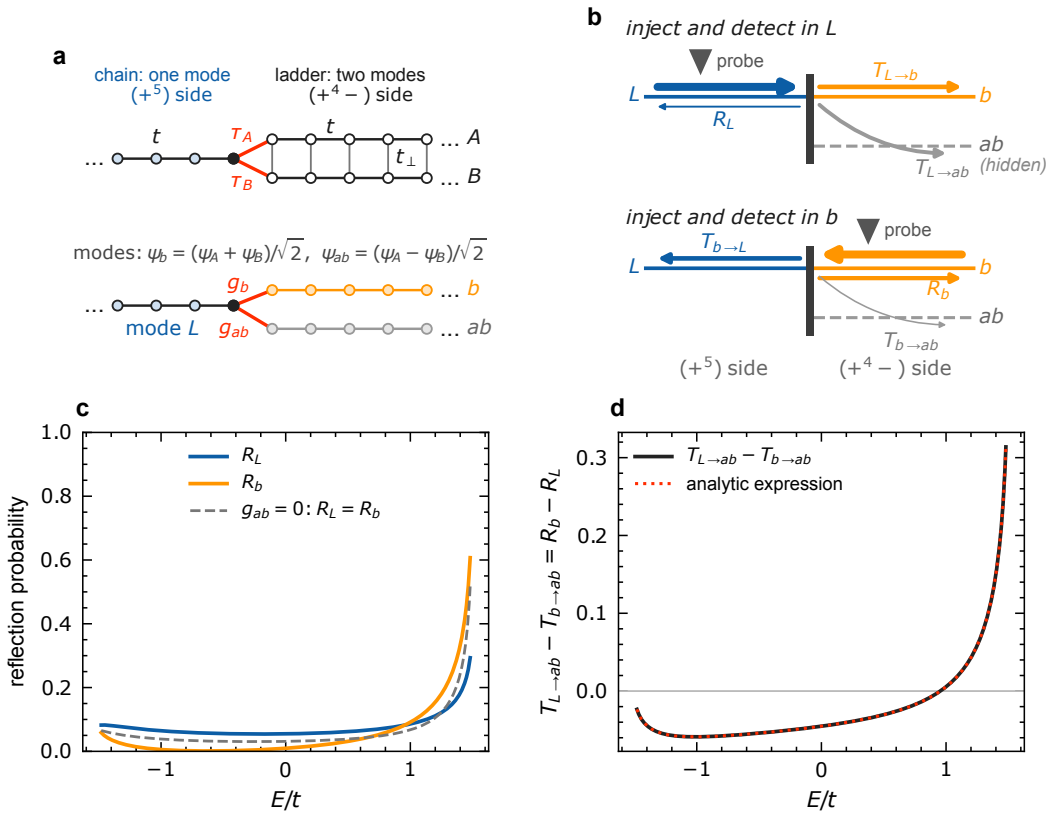


Figure S7: **Minimal scattering model.** **(a)** A single chain (one mode, L) joined to a two-leg ladder (two modes) by the hoppings τ_A and τ_B; in the basis of the symmetric (b) and antisymmetric (ab) combinations of the two legs, the junction is three single-mode chains meeting at one site, with couplings g_b and g_{ab}, Eq. (S4). **(b)** Scattering as seen by a probe coupled to L on the left and to b on the right, with ab hidden (dashed line); in the junction, L is band II of the $(+^5)$ side, b the Dirac cone and ab the hidden band V of the $(+^4-)$ side. The arrow widths depict the experimental case: the probed reflections R_L and R_b differ, and the difference is carried by the leaks $T_{L\to ab}$ and $T_{b\to ab}$ into the hidden channel, Eq. (S7). **(c)** Reflection probabilities $R_L(E)$ and $R_b(E)$ from the exact solution, for $t_\perp = 0.5t$, $\tau_A = 1.2t$, $\tau_B = 0.4t$ (solid lines), over the energy window in which all three channels propagate. For $\tau_A = \tau_B$ (same g_b) the hidden channel decouples and the two reflections coincide (dashed line). **(d)** The leak difference $T_{L\to ab} - T_{b\to ab}$ (line), which by Eq. (S7) is equal to the reflection difference $R_b - R_L$, coincides with the analytic expression of Eq. (S9) (dotted line); the sign of the asymmetry changes with energy.

Their moduli give the asymmetry in analytic form,

$$R_b - R_L = \frac{4g_{ab}^2 \sin k_{ab}}{|D|^2} \left(t^2 \sin k_L - g_b^2 \sin k_b\right). \tag{S9}$$

The asymmetry is proportional to g_{ab}^2, and its sign changes with energy where $t^2 \sin k_L = g_b^2 \sin k_b$. The group velocities of the channels, proportional to $\sin k_\sigma$, set the magnitude and the sign of the asymmetry, but cannot cause it by themselves: transmissions computed from the group velocities alone are the same in the two directions (Section III of the Supplementary Information of Ref.[12]). Figure S7c,d shows the exact solution for a representative set of parameters: the two reflection probabilities, and the leak difference $T_{L\to ab} - T_{b\to ab}$, equal to $R_b - R_L$ by Eq. (S7), which coincides with the analytic expression of Eq. (S9).

Parallel with the domain wall

In this minimal model, we artificially forced the mode selection. This mode selection happens in STM because the wave function of the STM tip couples mostly to the top graphene layer states, and the sample states vary in their localization on the graphene layers. Some, like the Dirac cone of the $\left(+^4-\right)$ phase are strongly layer polarized, with wave function weight mostly on the top layer, whereas the states of the $\left(+^5\right)$ area are delocalized over the whole sample. Furthermore, the second band in the $\left(+^4-\right)$ region (marked V in Fig. 4 of the main text) barely has any wave function weight on the top graphene layer. It is essentially decoupled from the STM tip. Because there is this strong difference in the layer polarization on the two sides of the domain wall (Fig. 4 of the main text), coupling to the top layer selects the modes. On the $\left(+^5\right)$ side the dispersive band (denoted II in Fig. 4 of the main text) of the top layer plays the role of L, the single mode in our minimal model. On the $\left(+^4-\right)$ side the flat band and its dispersive part are the hidden mode ab, and the states of the Dirac cone correspond to b (marked VI in Fig. 4 of the main text). The coupling g_{ab} is analogous to the ability of the wall to connect a top-layer mode to a hidden one, the layer polarization mismatch discussed in the main text.

In the experiment R_b is large, the interference fringes of the Dirac cone on the $\left(+^4-\right)$ side, and R_L is small, the featureless $\left(+^5\right)$ side. By Eq. (S7) this requires $T_{L\to ab} > T_{b\to ab}$:

the wave arriving from band II of the $(+^5)$ side is transmitted into the hidden band V of the $(+^4-)$ side more than the Dirac wave is converted into that band on reflection. The geometry of the model is the same as that of the junction: the hidden mode lies on the same side as the probed Dirac mode. The leak $T_{L\to ab}$ is therefore a transmission across the wall into a band without top-layer weight, and the leak $T_{b\to ab}$ a reflection into it. A reflection of the $(+^5)$-side wave into states without top-layer weight would also be invisible to the tip, but the layer-resolved calculation (Fig. 3 of the main text) shows no interference in any layer of the $(+^5)$ region, so the flux missing from R_L is transmitted, as in the model.

The reflection $R(E)$ of the wave packet calculation (Fig. 4c of the main text) counts all channels, whereas the STM measures R_L and R_b. In the three-channel picture the two are related as follows. Let $R_{(+^4-)}$ and $R_{(+^5)}$ denote the two curves of Fig. 4c, the reflection of the wave packet incident from the $(+^4-)$ and from the $(+^5)$ side. The lead on the $(+^4-)$ side populates the Dirac mode b, and $R_{(+^4-)}$ counts all of the current that is not transmitted into the far domain, including the part converted into the hidden band on reflection, $R_{(+^4-)} = 1 - T_{b\to L} = R_b + T_{b\to ab}$. The lead on the $(+^5)$ side populates band II, so $R_{(+^5)} = 1 - T_{L\to b} - T_{L\to ab} = R_L$. Reciprocity, $T_{L\to b} = T_{b\to L}$, then expresses both transmissions across the wall through the two curves,

$$T_{L\to b} = T_{b\to L} = 1 - R_{(+^4-)}, \qquad T_{L\to ab} = R_{(+^4-)} - R_{(+^5)}. \tag{S10}$$

At energies above and below the flat band, where band II disperses, Fig. 4c gives $R_{(+^4-)} \approx 0.9$ and $R_{(+^5)} \approx 0$. About one tenth of the current therefore crosses the wall between the Dirac cone and band II, in either direction, and nine tenths of the current arriving in band II continue into the hidden band V, below the surface of the $(+^4-)$ side. A wave arriving in band V from the $(+^4-)$ side crosses the wall with the same probability, $T_{ab\to L} = T_{L\to ab} \approx 0.9$. Summed over the channels, the transmission across the wall is the same in the two directions, $T_{L\to b} + T_{L\to ab} = T_{b\to L} + T_{ab\to L}$, close to one channel's worth here. For equal occupations on the two sides the currents cancel channel by channel and no net current flows across the wall: the wall is a one-way mirror for the probed modes only. The same bookkeeping applies to the lead on the bottom graphene layer (Fig. S6): it populates the

pentalayer band in place of the Dirac cone, so the probe addresses the channel that crosses the wall, and the reflection asymmetry is strongly reduced.

A charge transport measurement between two contacts that touch only the top layer, one on each side of the wall, does not result in a conductance asymmetry. In linear response the conductance is one number for both current directions, being proportional to the transmission T_{AB} between the two contacts (A, B), and unitarity of a two-terminal S matrix gives $T_{AB} = T_{BA}$ for any scatterer. In a closed ballistic sample the current sent into band V ends up in one of the two contacts after conversion at the edges or at the contact region, and with equal numbers of modes in the two leads this restores $R_A = R_B$, Eq. (S3). The asymmetry becomes observable in charge transport when band V is coupled to a third terminal. This can happen through a contact that couples to the bottom layer or to all layers of the $\left(+^4-\right)$ side. Current injected from the top contact of the $\left(+^5\right)$ side then arrives mostly at this third contact, $T_{L\to ab} \approx 0.9$, whereas current injected from the top contact of the $\left(+^4-\right)$ side mostly returns to its own contact, with $T_{b\to L} \approx 0.1$ reaching the opposite side. This is routing of the two inputs to different outputs, as in the photonic gratings that send the two incidence directions into different diffraction orders[13;14], and every pairwise transmission remains symmetric, $T_{\alpha\beta} = T_{\beta\alpha}$[9].

References

[1] Pálinkás, A. *et al.* Identification of graphite with perfect rhombohedral stacking by electronic raman scattering. *Carbon* **230**, 119608 (2024). URL https://doi.org/10.1016/j.carbon.2024.119608. 2401.17779.

[2] Nemes-Incze, P. zrbyte/ramantools: v0.3.1, DOI: 10.5281/zenodo.10143138 (2023). URL https://doi.org/10.5281/zenodo.10143138.

[3] Zhang, Y., Brar, V. W., Girit, C., Zettl, A. & Crommie, M. F. Origin of spatial charge inhomogeneity in graphene. *Nat. Phys.* **5**, 722–726 (2009). URL https://doi.org/10.1038/nphys1365.

[4] Sarsfield, P. J., Garcia-Ruiz, A. & Fal'ko, V. I. Substrate, temperature, and magnetic field dependence of electric polarization in mixed-stacking tetralayer graphenes. *Phys. Rev. Res.* **6** (2024). URL https://doi.org/10.1103/physrevresearch.6.043324.

[5] Seifert, E. J., Akyuz, E., Feenstra, R. M. & Hunt, B. M. Increasing flatness of surface bands of multilayer rhombohedral graphite with crystal thickness. *Phys. Rev. B.* **110**, L241407 (2024). URL https://doi.org/10.1103/physrevb.110.l241407.

[6] Garraway, B. M. & Suominen, K.-A. Wave-packet dynamics: new physics and chemistry in femto-time. *Reports on Progress in Physics* **58**, 365–419 (1995). URL https://doi.org/10.1088/0034-4885/58/4/001.

[7] Márk, G. I., Vancsó, P. & Mayer, A. New local pseudopotential for multilayer carbon materials and its application in wave packet dynamics. *Carbon Trends* **13**, 100310 (2023). URL https://doi.org/10.1016/j.cartre.2023.100310.

[8] Datta, S. *Electronic Transport in Mesoscopic Systems* (Cambridge University Press, Cambridge, 1995). URL https://doi.org/10.1017/CBO9780511805776.

[9] Büttiker, M. Four-terminal phase-coherent conductance. *Phys. Rev. Lett.* **57**, 1761–1764 (1986). URL https://doi.org/10.1103/PhysRevLett.57.1761.

[10] Buttiker, M. Symmetry of electrical conduction. *IBM J. Res. Dev.* **32**, 317–334 (1988). URL https://doi.org/10.1147/rd.323.0317.

[11] Maznev, A., Every, A. & Wright, O. Reciprocity in reflection and transmission: What is a 'phonon diode'? *Wave Motion* **50**, 776–784 (2013). URL http://dx.doi.org/10.1016/j.wavemoti.2013.02.006.

[12] Márk, G. I., Szendrő, M., Mayer, A., Simon, Z. & Vancsó, P. Robust reflection asymmetry across rhombohedral—bernal stacking boundaries in trilayer graphene. *Carbon Trends* **21**, 100589 (2025). URL https://doi.org/10.1016/j.cartre.2025.100589.

[13] Serebryannikov, A. E. One-way diffraction effects in photonic crystal gratings made of isotropic materials. *Physical Review B* **80** (2009). URL http://dx.doi.org/10.1103/PhysRevB.80.155117.

[14] Foteinopoulou, S. Breaking transmission symmetry without breaking reciprocity in linear all-dielectric polarization-preserving metagratings. *Physical Review Applied* **17**, 024064 (2022). URL https://doi.org/10.1103/PhysRevApplied.17.024064.